Nano Research
DOI 10.1007/s12274-016-1163-1
Research Article
ISSN 1998-0124
CN 11-5974/O4

Immobilization of NiS nanoparticles on N-doped carbon fiber aerogels as advanced electrode materials for supercapacitors

Youfang Zhang[1], Lizeng Zuo[1], Longsheng Zhang[1], Jiajie Yan[1], Hengyi Lu[1], Wei Fan[2] (✉), and Tianxi Liu[1,2] (✉)

[1] *State Key Laboratory of Molecular Engineering of Polymers, Department of Macromolecular Science, Fudan University, 220 Handan Road, Shanghai 200433, China*
[2] *State Key Laboratory of Modification of Chemical Fibers and Polymer Materials, College of Materials Science and Engineering, Donghua University, 2999 North Renmin Road, Shanghai 201620, China*

Received: 4 April 2016
Revised: 25 May 2016
Accepted: 27 May 2016

KEYWORDS
NiS,
cotton wool,
carbon fiber aerogels,
N-doping,
supercapacitors

ABSTRACT

NiS nanoparticles (NPs) with excellent electrochemical capacitance have attracted considerable attention as cost-effective energy-storage materials for supercapacitors in recent years. Preventing the aggregation and increasing the conductivity of NiS NPs are key to fully realizing their excellent electrochemical properties. In this work, NiS/N-doped carbon fiber aerogel (N-CFA) nanocomposites were obtained easily through the combination of polymerization, carbonization, and a one-step solvothermal reaction. N-CFA derived from polydopamine (PDA)-coated cotton wool was used as a template for the construction of hierarchical NiS/N-CFA nanocomposites, in which NiS NPs are uniformly immobilized on the surface of N-CFA. In this nanostructured system, N-CFA containing abundant nanofibers not only provides active regions for the growth of NiS NPs to prevent their aggregation, but also offers short pathways for the transport of electrons and ions. The electrochemical properties of the obtained NiS/N-CFA nanocomposites were investigated by cyclic voltammetry, galvanostatic charge–discharge, and alternating current impedance measurements. The optimized NiS/N-CFA nanocomposite exhibits a high specific capacitance of 1,612.5 $F \cdot g^{-1}$ at a charge/discharge current density of 1 $A \cdot g^{-1}$ and excellent rate capacitance retention of 66.7% at 20 $A \cdot g^{-1}$. The excellent electrochemical properties of NiS/N-CFA nanocomposites make these materials promising electrode materials for supercapacitors.

1 Introduction

Supercapacitors with unique properties such as fast charge/discharge rates, high power densities, and long cycle lives have been considered to be promising candidates for future energy-storage devices [1, 2]. Based

Address correspondence to Wei Fan, weifan@dhu.edu.cn; Tianxi Liu, txliu@fudan.edu.cn, txliu@dhu.edu.cn

on their energy-storage mechanisms, supercapacitors can be divided into electrical double-layer capacitors (EDLCs) and electrochemical pseudocapacitors (EPCs). EDLCs store their capacitance via reversible ion absorption and charge separation at the electrode/electrolyte interface, whereas EPCs store the energy by fast and reversible faradaic redox reactions at the surfaces of electro-active materials. Therefore, EDLCs are mainly based on carbon materials with good electrical conductivity and excellent stability but relatively low specific capacitance [3–5]. Unlike EDLCs, EPCs are mainly based on active pseudocapacitive materials with high specific capacitance but relatively poor stability [6–8]. Thus, combining EDLCs with EPCs is an effective strategy to enhance the specific capacitance, power and energy densities, and cyclic performance of supercapacitors [9–11].

As typical pseudocapacitive materials, metal sulfides such as NiS_x [12–17], CoS_x [18], $CoNi_2S_4$ [19], $NiCo_2S_4$ [20–22], and WS_2 [23] have been extensively investigated as supercapacitors because of their excellent pseudocapacitive performance. Among them, NiS, which is low cost, non-toxic, and abundant on earth and has high redox activity, is emerging as a promising energy-storage material [24–26]. For instance, Wang et al. [27] fabricated one-dimensional (1D), [110]-oriented NiS nanorods with a high specific capacitance of 1,403.8 $F \cdot g^{-1}$ at a current density of 1 $A \cdot g^{-1}$ because of the designed 1D electron-transport pathway and large specific surface area. Additionally, Yang et al. [28] prepared a unique flower-like β–NiS architecture comprising a pine tree-like nanostructure surrounded by abundant nano-branches. This hierarchical structure increased the material's surface area, thereby increasing the number of contact opportunities for electrolyte and electrode materials. In addition, the rich nano-branches help to shorten the diffusion paths of the electrolyte ions and the charge-transport pathways. Thus, this flower-like β-NiS exhibits excellent electrochemical performance for supercapacitors. However, poor conductivity and self-aggregation of NiS nanoparticles (NPs) substantially hinder their electrochemical performance. To overcome these issues, the preparation of uniformly distributed NiS NPs on a conductive substrate is an effective strategy to enhance their electrochemical performance as electrode materials in supercapacitors.

Currently, considerable research focuses on conductive substrates made of carbon materials, including activated carbon [29], graphene [30–33], carbon nanotubes (CNTs) [34–37], carbon nanofibers [38], mesoporous carbon [25, 39], and carbon cloth [40]. For example, bacteria-reduced graphene oxide (GO)-NiS (BGNS) networks with submillimeter pores could facilitate the electrolyte access and promote the migration of ions and charges. Compared with stacked reduced GO-NiS prepared without the aid of bacteria, BGNS, which has a unique nm–μm structure, exhibited a higher specific capacitance of approximately 1,424 $F \cdot g^{-1}$ at a current density of 0.75 $A \cdot g^{-1}$ and a specific capacitance of 406 $F \cdot g^{-1}$ at a high current density of 75 $A \cdot g^{-1}$ [41]. In another work, CNTs were utilized as a 1D backbone for uniform immobilization of Ni_3S_2 nanosheets. In this hybridized system, the CNTs served as the electron acceptor, accelerating the migration of charges and ions and retarding charge recombination. Simultaneously, ultrathin Ni_3S_2 nanosheets, which had large surface areas, could fully expose their active edge sites, thereby enhancing the capacitance and achieving good cycling stability [34]. However, most previous studies have focused on carbon materials with flat structures such as 1D or two-dimensional (2D) structures and the use of three-dimensional (3D) backbones to grow NiS NPs has rarely been reported.

Carbon aerogels (CAs), which have 3D porous nanostructures with large surface areas and high electrical conductivities, can be used as excellent templates for the growth of NPs with high electrochemical activities. Generally, ~~CA preparation~~ involves three (for CAs derived from GO [42–45], CNTs [46, 47], or GO nanoribbons [48, 49]) or four (for CAs derived from organic materials [50, 51]) basic steps: sol–gel transition, network perfection, gel–aerogel transition, and carbonization [52]. Completing these steps, especially the sol–gel and gel–aerogel transitions, is time consuming and usually takes several days or longer. In contrast, CAs derived from biomass materials such as bacterial cellulose [53] and cotton wool [54] can be directly prepared via carbonation without any other procedures. Among these biomass materials, cotton wool is rich in fibers and, thus, it has a 3D interconnected and conductive fiber framework. This

fiber framework can not only prevent the aggregation of activated NPs, but also favor the transport of electrons and charges and accelerate the access of electrolyte ions to activated NPs. In addition, introducing heteroatoms (e.g., N, P, or S) into carbon materials can provide an electron donor and accelerate the mobility of charges, thereby enhancing the material capacitance [55–57].

Herein, N-doped carbon fiber aerogels (N-CFAs), which are lightweight and have high porosity, are prepared by carbonizing polydopamine (PDA)-coated cotton wool. Subsequently, the obtained N-CFA is used as a 3D conductive backbone for the *in situ* growth of irregular NiS NPs via a facile hydrothermal method. In this hierarchical structure, the abundant fibers create 3D interconnected conductive networks, which can prevent the aggregation of NiS NPs, favor the transport of electrons and charges, and accelerate the access of electrolyte ions to NiS NPs. Consequently, the optimized NiS/N-CFA nanocomposite exhibits excellent electrochemical performance with high specific capacitance and good capacitive retention after 5,000 cycles compared to that of pure NiS NPs, making it a promising electrode material for supercapacitors.

2 Experimental

2.1 Preparation of N-CFA

The PDA-coated cotton wool was prepared according to previously reported methods [58]. First, 2 g cylindrically shaped pieces of cotton wool were immersed in an aqueous solution of dopamine (DA; 1 mg·mL^{-1} in 10 mM Tris-buffer, pH = 8.5) under mild stirring at 70 °C for PDA coating. After 4 h, the resulting products were collected with tweezers and washed several times with deionized (DI) water to remove any byproducts. The final products, named N-CFAs, were obtained after drying at 80 °C for 6 h and subsequent carbonization at 800 °C for 2 h with a ramping rate of 5 °C·min^{-1} under a N_2 atmosphere. For comparison, CFA was prepared via the same carbonization procedure without any treatment of the cotton wool.

2.2 Preparation of NiS/N-CFA nanocomposites

NiS/N-CFA nanocomposites with various mass loadings of NiS were prepared by a one-step solvothermal reaction. Briefly, 2 mmol of Ni acetate and 4 mmol of thiourea were dispersed in 30 mL of a mixed solvent of dimethylformamide (DMF) and DI water (volume ratio of 1:2). Then, 50 mg of N-CFA was added to the above solution. Subsequently, the mixture was transferred into a 40 mL ~~Teflon stain~~ ~~steel autoclave~~ and reacted at 180 °C for 12 h. The resulting products were collected with tweezers and washed several times with DI water. The final products were obtained after drying at 80 °C for 6 h and named NiS/N-CFA-2. Additional NiS/N-CFA nanocomposites were created using 4, 6, and 8 mmol of Ni acetate solution and denoted as NiS/N-CFA-4, NiS/N-CFA-6, and NiS/N-CFA-8, respectively. For comparison, pure NiS NPs were also prepared via the same procedure without

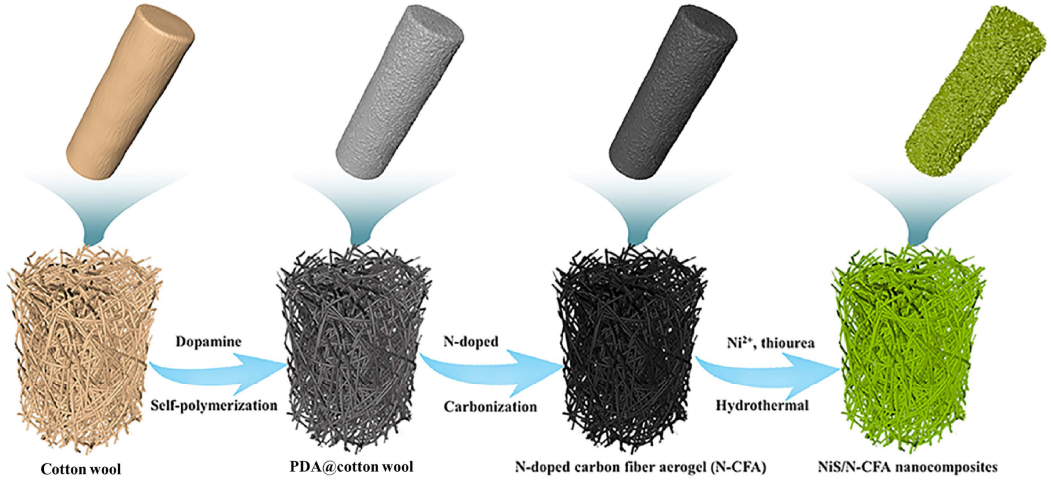

Scheme 1 Schematic illustration of the preparation of NiS/N-CFA nanocomposites.

the addition of N-CFA, and NiS/CFA-6 nanocomposite was obtained via the same procedure with CFA derived from pure cotton wool.

2.3 Characterization

The morphologies of the products prepared in this work were characterized by field-emission scanning electron microscopy (FESEM) (Ultra 55, Zeiss) at an acceleration voltage of 5 kV, and their chemical compositions were investigated with energy-dispersive X-ray spectroscopy (EDS). The Fourier transform infrared spectra (FTIR) of raw cotton wool and PDA@cotton wool were measured on a Nicolet 6700 FTIR spectrometer. X-ray diffraction (XRD) experiments were conducted from 2θ = 5° to 80° on an X'Pert Pro X-ray diffractometer with CuKα radiation (λ = 0.1542 nm) under a voltage of 40 kV and a current of 40 mA. X-ray photoelectron spectroscopy (XPS) analyses were performed with a VG ESCALAB 220I-XL instrument. All XPS spectra were corrected using the C 1s line at 284.6 eV, and curve fitting and background subtraction were accomplished using XPS PEAK41 software. Thermogravimetric analysis (TGA; Pyris 1 TGA) was performed under air flow from 100 to 800 ℃ at a heating rate of 20 ℃·min^{-1}.

2.4 Electrochemical characterization

All electrochemical measurements, including cyclic voltammetry (CV), galvanostatic charge–discharge curves, and electrochemical impedance spectroscopy (EIS) were conducted in 2 mol·L^{-1} KOH electrolyte with typical three-electrode cells (Pt wire as the counter electrode, Ag/AgCl as the reference electrode, and Ni foam-supported NiS/N-CFA nanocomposites as the working electrode). The working electrodes were prepared according to our previous work [48]. CV curves were collected over a voltage range from 0 to 0.5 V, and galvanostatic charge–discharge curves were measured over a voltage range from 0 to 0.4 V. EIS was recorded in the frequency range from 0.01 to 100 kHz at an open-circuit potential with an amplitude of 5 mV.

3 Results and discussion

Figure 1(a) shows a digital photo of a cotton wool sample before and after carbonization. After pyrolysis, the volume of the CFA is much smaller than that of the raw cotton wool, and its weight is only 10% of that of cotton wool. As shown in Fig. S1(b) in the Electronic Supplementary Material (ESM), the CFA can be supported by a blade of green grass, confirming its low density. The structure of cotton wool consists of twisted fibers with diameters ranging from tens of nanometers to several micrometers (Fig. S1(c) in the ESM). The rich oxygen-containing groups, including hydroxyl and carboxylic acid groups, present in cotton wool could interact with the amine groups of DA, thereby facilitating the uniform and rapid *in situ* polymerization of PDA on the fiber surface of cotton wool. As indicated in Fig. S2 in the ESM, the color of

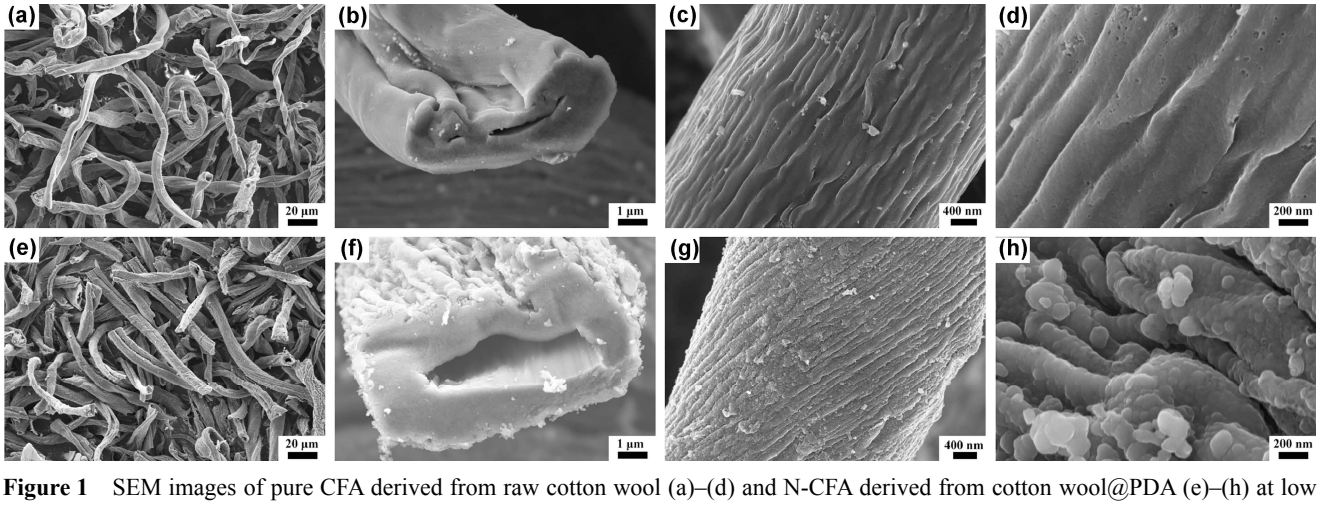

Figure 1 SEM images of pure CFA derived from raw cotton wool (a)–(d) and N-CFA derived from cotton wool@PDA (e)–(h) at low and high magnifications.

the cotton wool changed from white to dark brown after immersion in DA solution, indicating the successful coating of PDA onto the raw cotton wool. However, the FTIR spectra (Fig. S3 in the ESM) revealed no significant differences between the raw cotton wool and PDA@cotton wool because PDA and raw cotton wool contain similar functional groups.

Figure 1 shows typical SEM images of the CFA derived from raw cotton wool (a)–(d) and the N-CFA derived from PDA@cotton wool (e)–(h). After carbonization, CFA exhibits an interconnected 3D structure of fibers similar to that of raw cotton wool, although the fiber diameter was slightly smaller. Close observation of a single fiber reveals an irregular cavity (Fig. 1(b)) on the cross section and abundant wrinkles and gullies on the surface (Figs. 1(c) and 1(d)). After subjecting the PDA-coated cotton wool to carbonization, N-CFA was successfully obtained. As shown in Figs. 1(f) and 1(g), the fiber surface of CFA became much coarser, and the gap between the wrinkles and gullies decreased. Close inspection reveals that some particle-like features appear on the fiber surface (Fig. 1(h)), indicating that PDA molecules covered the fiber surface of the cotton wool. The EDS results of N-CFA (Fig. S4 in the ESM) further confirm that N is uniformly distributed on the N-CFA, whereas no N was observed on the CFA (Fig. S5 in the ESM). The coarse surfaces of N-CFA fibers allow NiS precursors to diffuse readily and be reduced *in situ* to NiS NPs on the surface of the CFA nanofibers. Therefore, N-CFA could serve as a template for the further growth of NiS NPs because of its rough N-containing layer.

Figure 2 shows typical images of NiS/N-CFA nanocomposites with different amounts of NiS NPs. Clearly, as the Ni salt concentration increases, the amount of NiS NPs grown on the surface of the N-CFA also gradually increases. As shown in Fig. 2(a), discrete NiS NPs are sparsely anchored on the surface of the N-CFA when the initial Ni salt dosage is 2 mM. The close observation of NiS/N-CFA-2 reveals that the NiS NPs are approximately triangle in shape with sharp corners (Fig. 2(b)). Increasing the initial Ni salt concentration to 4 mM results in the uniform coverage of the fibers of the N-CFA with NiS NPs, as displayed in Fig. 2(c). However, the surface of the fibers can be

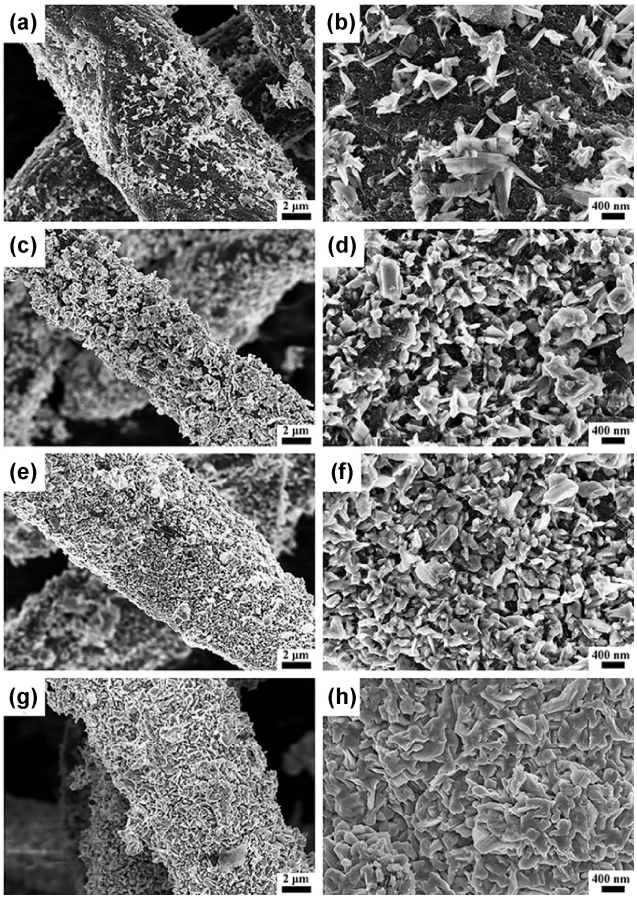

Figure 2 SEM images of NiS/N-CFA-2 ((a) and (b)), NiS/N-CFA-4 ((c) and (d)), NiS/N-CFA-6 ((e) and (f)), and NiS/N-CFA-8 ((g) and (h)) at low and high magnifications.

clearly seen in the SEM image at high magnification (Fig. 2(d)) because of the low amount of Ni salt. When the Ni salt concentration is further increased to 6 mM, the fibers of the N-CFA become uniformly and fully covered by NiS NPs (Figs. 2(e)–2(f)). However, when this concentration is increased to 8 mM, the NiS NPs grow so densely that some aggregates inevitably appear, which would hinder the interactions between the N-CFA and NiS NPs (Figs. 2(g)–2(h)). For pure NiS without the N-CFA template (Fig. S6 in the ESM), the NiS NPs self-agglomerate into hydrangea-like morphologies, greatly decreasing the exposure of the NiS active sites. For comparison, NiS/CFA-6 was also prepared via the same procedure with pure CFA derived from raw cotton wool. As shown in Fig. S7 in the ESM, the surface of the CFA was also uniformly covered with NiS NPs.

The crystal structures of pure NiS NPs, N-CFA,

and NiS/N-CFA-6 were investigated using their XRD patterns. As shown in Fig. 3, for both pure NiS NPs and NiS/N-CFA-6, the diffraction peaks at 2θ = 18.9°, 30.8°, 32.7°, 36.2°, 37.9°, 41.0°, 49.3°, 50.7°, 53.1°, 57.9°, 60.1°, 66.8°, 68.2°, 73.5°, and 76.1° correspond to the (110), (101), (300), (021), (220), (211), (131), (410), (401), (330), (012), (103), (200), (112), and (202) planes, respectively, which can be easily indexed to β-NiS. In the N-CFA sample, the wide, significant peak at approximately 2θ = 26° and the weak peak at approximately 2θ = 44° can be assigned to the (002) and (100) planes (JCPDS No. 01-0646), respectively, indicating that the obtained N-CFA possesses low crystallinity. All of these results suggest that the N-CFA substrate does not affect the crystallinity of the NiS NPs. Additionally, the XRD results confirm that β-NiS NPs were successfully grown on the surface of the N-CFA.

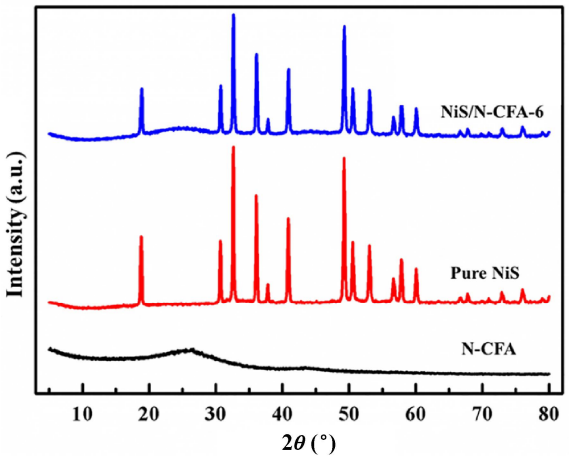

Figure 3 XRD patterns of pure NiS NPs, N-CFA, and NiS/N-CFA-6.

To further examine the elemental compositions and chemical states of NiS/N-CFA, XPS measurements were performed. As shown in Fig. 4(a), the survey spectrum indicates the co-existence of C, N, O, Ni, and S elements in NiS/N-CFA, without any detectable impurities. The high-resolution spectrum of N 1s was characterized to analyze the bonding configurations of N atoms in the NiS/N-CFA sample. Figure 4(b) shows that the peak deconvolution of N 1s is mainly reflected by three peaks centered at 398.5, 400.0, and 401.3 eV, corresponding to pyridinic-N (N-6), pyrrolic-N (N-5), and quaternary-N (N-Q), respectively. As reported previously [57–59], in electrode materials, N-6 and N-5 are electrochemically active, contributing to the enhancement of the materials' capacitances.

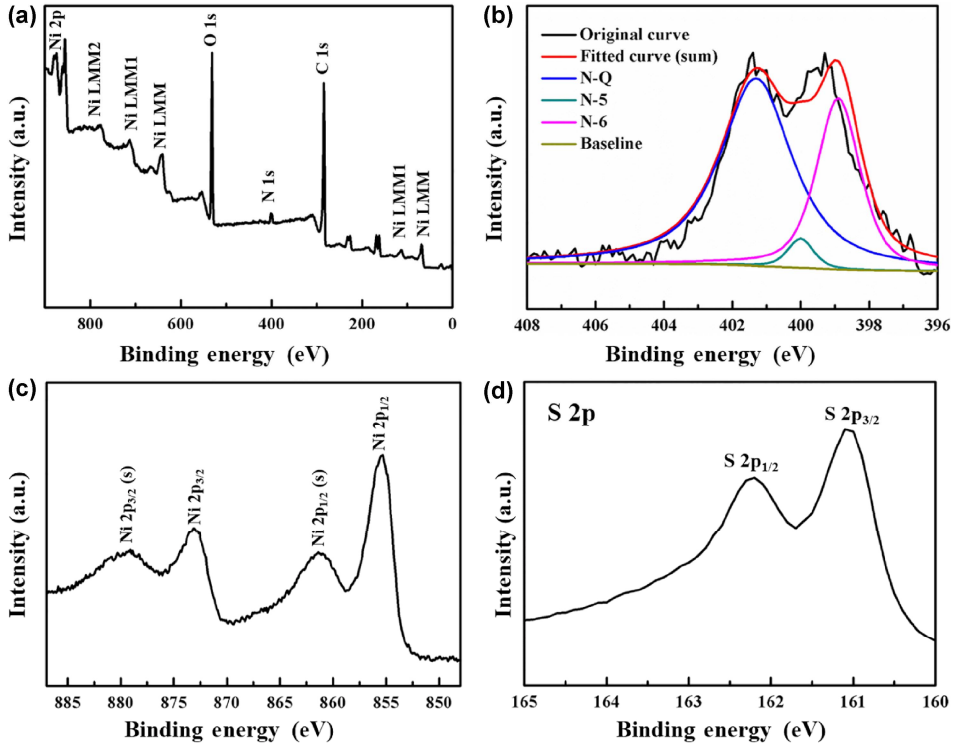

Figure 4 XPS survey spectrum (a), N 1s spectrum (b), Ni 2p spectrum (c), and S 2p spectrum (d) of NiS/N-CFA-6.

N-6 offers a lone electron pair for conjugation with the p-conjugated rings, and N-5 provides electron-donor characteristics that enhance the charge and electron mobility. The high-resolution Ni 2p spectrum (Fig. 4(c)) exhibits two characteristic peaks at 855.5 and 873.2 eV (with a spin-energy separation of 17.7 eV), corresponding to Ni $2p_{3/2}$ and Ni $2p_{1/2}$, respectively. Furthermore, the associated satellites of Ni $2p_{3/2}$ and Ni $2p_{1/2}$ are located at 861.4 and 879.1 eV, respectively, which is characteristic of Ni^{2+}. In addition, the high-resolution S 2p spectrum (Fig. 4(d)) shows two peaks centered at 162.4 and 161.1 eV, indicating the existence of divalent sulfide ions (S^{2-}). Thus, the XPS results also suggest that NiS NPs were successfully grown on the surface of the N-CFA.

The loading amounts of NiS NPs in the NiS/N-CFA nanocomposites were calculated based on their TGA curves (Fig. 5) and were 22.6 wt.%, 32.5 wt.%, 36.6 wt.%, and 39.6 wt.% for the NiS/N-CFA-2, NiS/N-CFA-4, NiS/N-CFA-6, and NiS/N-CFA-8 nanocomposites, respectively. The loading amounts of NiS NPs in the NiS/CFA nanocomposite was also calculated from the TGA curve (Fig. S8 in the ESM) and was 34.8 wt.%, which is close to that of NiS/N-CFA-6.

To investigate the electrochemical performance of NiS/N-CFA nanocomposites, CV curves and galvanostatic charge–discharge curves were collected in 2 M KOH aqueous electrolyte. As shown in Fig. 6(a), the typical CV curves of pure NiS NPs and NiS/N-CFA nanocomposites obtained with a scan rate of 10 $mV \cdot s^{-1}$ show two peaks (e.g., an anodic peak and a cathodic peak) in the potential range from 0 to 0.5 V,

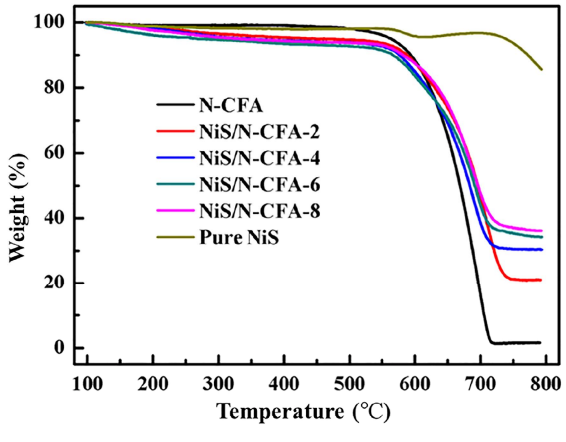

Figure 5 TGA curves of N-CFA, pure NiS NPs, and all NiS/N-CFA nanocomposites.

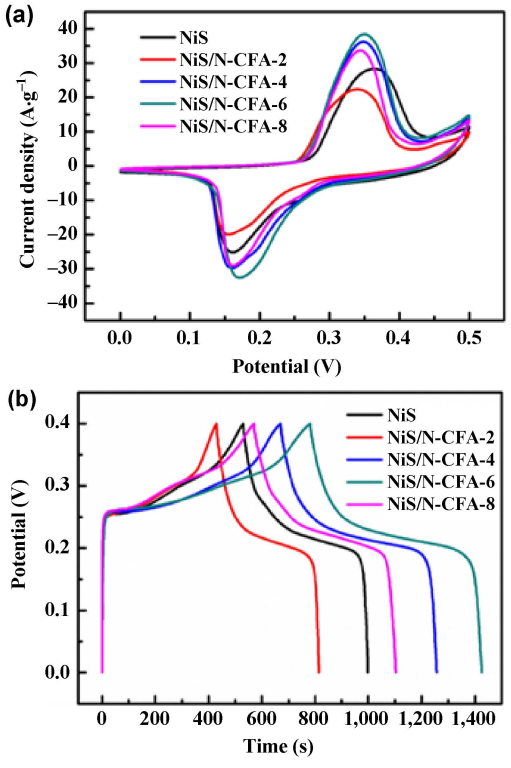

Figure 6 CV curves collected at a scan rate of 10 $mV \cdot s^{-1}$ (a) and galvanostatic charge–discharge curves measured at a current density of 1 $A \cdot g^{-1}$ (b) for pure NiS NPs and all NiS/N-CFA nanocomposites.

which reflect the materials' pseudocapacitive characteristics. The related energy-storage mechanism of the NiS/N-CFA nanocomposites is mainly associated with the following reversible processes involving faradaic redox reactions among NiS, NiSOH, and NiSO in alkaline electrolyte

$$NiS + OH^- \leftrightarrow NiSOH + e^- \quad (1)$$

$$NiSOH + OH^- \leftrightarrow NiSO + e^- \quad (2)$$

Close inspection of Fig. 6(a) reveals that NiS/N-CFA nanocomposites exhibit larger CV areas and higher current densities than pure NiS NPs, indicating that the electrochemical performance can be greatly enhanced by using N-CFA as the conductive substrate. In addition, NiS/N-CFA-6 showed the highest capacitance among the samples, and its remarkably enhanced electrochemical performance is attributable to the synergistic effects of 3D, conductive N-CFA with electric double-layer capacitance and uniformly distributed NiS NPs with high pseudocapacitance. Figure 6(b) shows the galvanostatic charge–discharge curves of pure NiS NPs

and NiS/N-CFA nanocomposites at a current density of 1 A·g^{-1}, which display distinct pseudocapacitive behaviors, in accordance with the CV curves. Clearly, NiS/N-CFA-6 exhibits the highest specific capacitance among the analyzed samples—1,612.5 F·g^{-1}—at a current density of 1 A·g^{-1}. For comparison, the electrochemical performance of NiS/CFA-6 prepared with pure CFA derived from raw cotton wool was also investigated. As shown in Fig. S9 in the ESM, NiS/CFA-6 shows pseudocapacitance in the potential range from 0 to 0.5 V. Moreover, the specific capacitance of NiS/CFA-6 calculated from its charge–discharge curve was 1,232.5 F·g^{-1} at a current density of 1 A·g^{-1}, which is lower than that of NiS/N-CFA-6. This difference indicates the significance of N doping.

To better understand the differences in the electrochemical performances of these materials for supercapacitors, the rate capabilities of pure NiS NPs and the optimized NiS/N-CFA-6 nanocomposite were investigated at various scan rates and current densities. As shown in Fig. 7(a), as the scan rate increases, the shapes of the CV curves of pure NiS NPs become deformed (at a scan rate of 50 mV·s^{-1}), and the redox peaks become seriously shifted and even disappear, indicating that pure NiS NPs have poor rate capability. Additionally, according to the curves in Figs. 7(b) and 7(c), the specific capacitances are 1,170.0, 987.5, 852.5, 736.2, and 585.0 F·g^{-1} at current densities of 1, 2, 5, 10, and 20 A·g^{-1}, respectively. That is, only 50% of the specific capacitance of pure NiS NPs is retained when the discharge current density increases from 1 to 20 A·g^{-1}. However, for NiS/N-CFA-6, the shape of the CV curves is retained well, and the current density increases as the scan rate increases from 5 to 50 mV·s^{-1}. This behavior suggests that employing N-CFA as a conductive template leads to good rate stability. According to Figs. 7(e) and 7(f), the specific capacitances are 1,612.5, 1,479.0, 1,379.4, 1,210.0, and 1,075.0 F·g^{-1} at current densities of 1, 2, 5, 10, and 20 A·g^{-1}, respectively. Thus, 66.7% of the specific capacitance of NiS/N-CFA-6 is retained as the discharge current density increases from 1 to 20 A·g^{-1}. Additionally, to the best of our knowledge, the specific capacitances of NiS/N-CFA-6 are comparable and even better than those of the NiS-based electrode materials reported in the literature (Table 1). The rate capabilities of NiS/CFA-6 nanocomposite at various scan rates and current densities are also given in Fig. S10 in the ESM. The shapes of all CV curves are well maintained, and the current density increases as the scan rate increases from 5 to 50 mV·s^{-1}. Furthermore, 67.7% of the specific capacitance of NiS/CFA-6 is retained as the discharge current density increases from 1 to 20 A·g^{-1}, which is comparable to

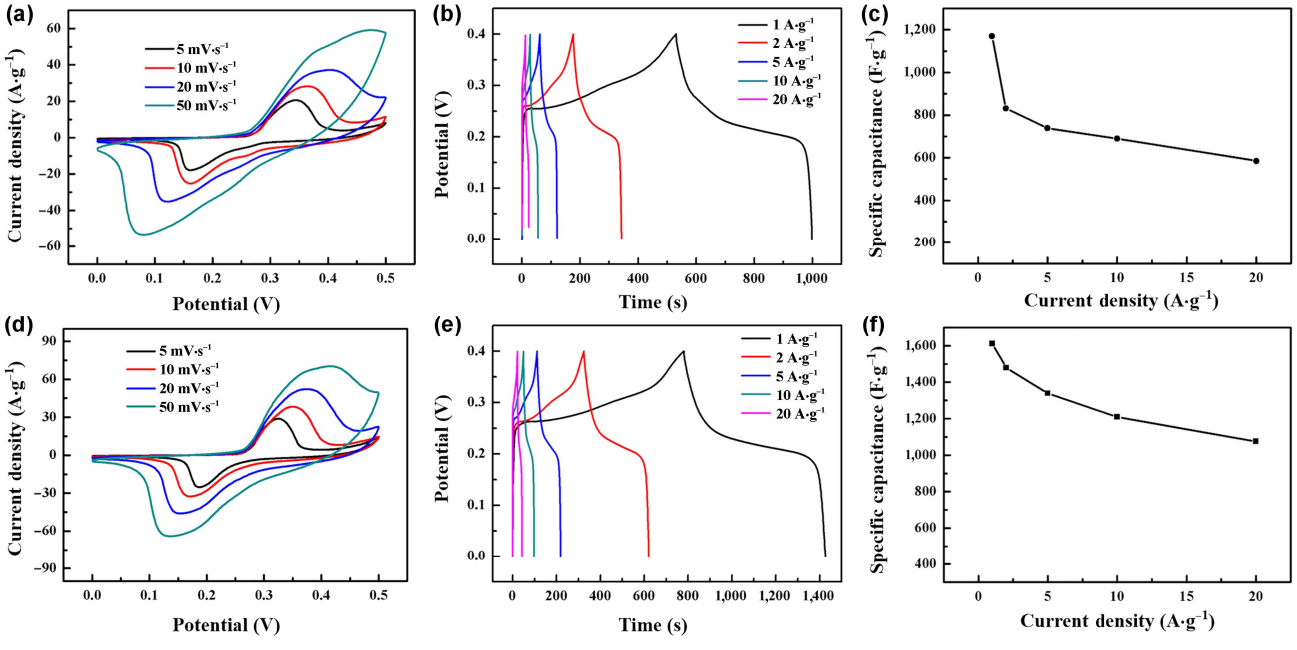

Figure 7 Rate capabilities of pure NiS (a)–(c) and NiS/N-CFA-6 nanocomposite (d)–(f) at various scan rates and current densities.

Table 1 Comparison of Ni_xS_y-based electrode materials for supercapacitors

Electrode	Electrolyte	Current dendity ($A \cdot g^{-1}$)	Specific capacitance ($F \cdot g^{-1}$)	Refs.
NiS/rGO	2 M KOH	0.50	905.3	[12]
NiS/rGO	2 M KOH	5.00	1,169.0	[14]
MCs[a]@GNS[b]/NiS	6 M KOH	0.50	775.0	[24]
NiS nanoframes	6 M KOH	1.00	2,112.0	[25]
NiS hollow spheres	2 M KOH	4.08	927.0	[26]
[110]-orientend NiS	6 M KOH	1.00	1,403.8	[27]
NiS/GO	6 M KOH	1.00	800.0	[31]
NiS/ERGO[c]	1 M KOH	2.00	1,392.2	[32]
NiS/rGO aerogel	6 M KOH	2.00	852.0	[33]
CNT@Ni_3S_2	2 M KOH	4.00	514.0	[34]
Ni_3S_2/MWCNT[d]	2 M KOH	3.20	800.0	[35]
NiS/SWNTs[e]	2 M KOH	5.00	1,110.0	[37]
Ni_3S_2/CNFs[f]	2 M KOH	2.00	833.0	[38]
BGNS[g]	2 M KOH	0.75	1,424.0	[41]
NiS/CRs[h]	2 M KOH	1.00	1,092.0	[60]
Flower-like NiS	2 M KOH	2.00	972.3	[61]
Ni_3S_4@MoS_2	6 M KOH	2.00	1,440.9	[62]
NiS/N-CFA	2 M KOH	1.00	1,612.5	This work

[a]MCs: make-up cottons; [b]GNS: graphene nanosheets; [c]ERGO: electrochemically reduced graphene oxide; [d]MWCNT: multiwalled carbon nanotubes; [e]SWNTs: single-wall carbon nanotubes; [f]CNFs: carbon nanofibers; [g]BGNS: bacteria-reduced graphene oxide-NiS; [h]CRs: carbon nanorods.

that observed for NiS/N-CFA-6. However, the specific capacitance of NiS/CFA-6 is much lower than that of NiS/N-CFA-6 at the same current densities. Therefore, NiS/N-CFA-6 is a promising candidate electrode material for supercapacitors.

Cycling stability is a very important factor for evaluating the electrochemical performance of electrode materials for supercapacitors. Therefore, cycling tests of NiS/N-CFA-6 and pure NiS NPs were performed by collecting CV curves while sweeping the potential from 0 to 0.5 V at a scan rate of 20 $mV \cdot s^{-1}$ for 5,000 cycles. As shown in Fig. 8(a), notably, the specific capacitances of NiS/N-CFA-6 and pure NiS NPs increase during the first 300 cycles because of the activation effect, which allows the confined ions to gradually diffuse outward. More importantly, NiS/N-CFA-6 retains approximately 87.0% of its initial capacitance after 5,000 cycles, whereas pure NiS NPs exhibit only 54.9% retention. As mentioned above, the unique 3D fiber network of N-CFA could enhance the electrical conductivity and thereby allow stable faradaic redox reactions involving the NiS NPs. In addition, N-CFA can act as a buffering substrate to accommodate the local volumetric expansion/contraction of the NiS NPs during long-term cycling.

EIS is an informative technique that can be used to evaluate the conductive properties and charge transport behaviors at the interface between electrode materials and an electrolyte. The Nyquist plots of pure NiS, N-CFA, and NiS/N-CFA nanocomposite electrodes are displayed in Fig. 8(b). In the high-frequency region, almost no semi-circle or inconspicuous arcs can be observed for N-CFA and NiS/N-CFA nanocomposites, whereas a clear quadrant is evident for pure NiS NPs. This finding indicates that using N-CFA as a conductive framework decreases the resistance at the electrode/electrolyte interface. In the low-frequency region, all samples show straight lines. Close inspection of these Nyquist plots reveals that the lines of the nanocomposite electrodes are more vertical than those

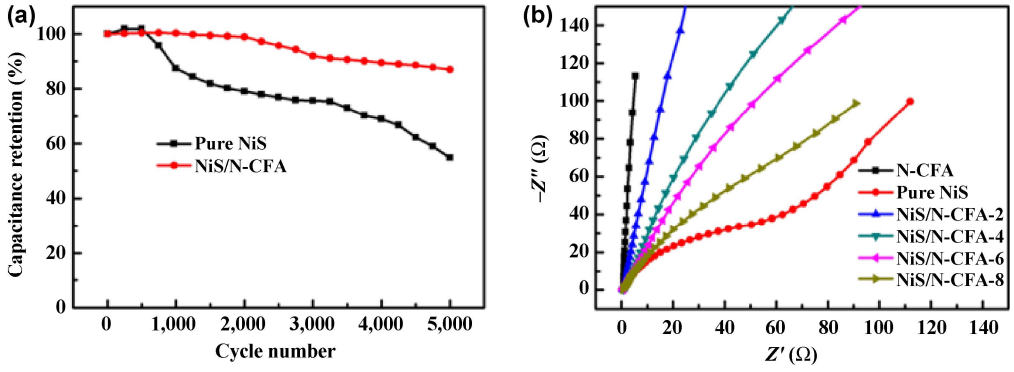

Figure 8 Cycling performances of pure NiS NPs and NiS/N-CFA-6 at a scan rate of 20 $mV \cdot s^{-1}$ for 5,000 cycles (a) and Nyquist plots of N-CFA, pure NiS NPs, and all NiS/N-CFA nanocomposites measured in a frequency range from 100 kHz to 0.01 Hz.

of pure NiS NPs, indicating that the nanocomposites have better capacitive behavior. Additionally, as the amount of N-CFA increases, the line becomes increasingly vertical, implying that the improved supercapacitive behavior can be attributed to fast ion diffusion in the electrode materials. Furthermore, the Nyquist plots show a more vertical line for the NiS/N-CFA-6 electrode than for the NiS/CFA-6 one (Fig. S11 in the ESM), indicating that the former's better capacitive behavior can be ascribed to N doping. All of these EIS results illustrate that the 3D nano-scaffold of N-CFA can facilitate the efficient diffusion of electrolyte ions to the electrode surface and shorten the electron-transport path, thereby enhancing the conductivity of NiS NPs.

4 Conclusions

In summary, NiS NPs anchored on the fiber surface of N-CFA were successfully fabricated by a simple hydrothermal method. The unique structure of the NiS/N-CFA nanocomposite offers a number of distinct advantages. First, N-CFA with abundant fiber networks was directly obtained via the carbonization of inexpensive and sustainable cotton wool coated with PDA without any complicated treatment. Second, N-CFA with a highly conductive fiber skeleton effectively prevented the aggregation of NiS NPs and helped to fully expose the active edge sites of NiS NPs. N-CFA also acts as a conductive substrate, enhancing the electron mobility and shortening the transport pathways of electrons and ions and thereby increasing the capacitance. Therefore, the optimal NiS/N-CFA nanocomposite electrode material exhibited excellent electrochemical performance for supercapacitors with a specific capacitance of 1,612.5 $F \cdot g^{-1}$ at a current density of 1 $A \cdot g^{-1}$ and good cycling stability. These results demonstrate that combining CFA with NiS NPs to generate hierarchical nanocomposites creates promising candidates energy-storage materials for supercapacitors.

Acknowledgements

The authors are grateful for the financial support from the National Natural Science Foundation of China (Nos. 51125011 and 51433001).

Electronic Supplementary Material: Supplementary material () available in the online version of this article at http://dx.doi.org/10.1007/ s12274-016-1163-1.

References

[1] Yan, J.; Wang, Q.; Wei, T.; Fan, Z. J. Recent advances in design and fabrication of electrochemical supercapacitors with high energy densities. *Adv. Energy Mater.* **2014**, *4*, 1300816.

[2] Zhang, L. Z.; Yu, J. C.; Mo, M. S.; Wu, L.; Li, Q.; Kwong, K. W. A general solution-phase approach to oriented nanostructured films of metal chalcogenides on metal foils: The case of nickel sulfide. *J. Am. Chem. Soc.* **2004**, *126*, 8116–8117.

[3] Ma, Y. W.; Li, P.; Sedloff, J. W.; Zhang, X.; Zhang, H. B.; Liu, J. Conductive graphene fibers for wire-shaped supercapacitors strengthened by unfunctionalized few-walled carbon nanotubes. *ACS Nano* **2015**, *9*, 1352–1359.

[4] Ghotbi, M. Y.; Azadfalah, M. Design of a layered nanoreactor to produce nitrogen doped carbon nanosheets as highly efficient material for supercapacitors. *Mater. Design* **2016**, *89*, 708–714.

[5] Feng, H. B.; Hu, H.; Dong, H. W.; Xiao, Y.; Cai, Y. J.; Lei, B. F.; Liu, Y. L.; Zheng, M. T. Hierarchical structured carbon derived from bagasse wastes: A simple and efficient synthesis route and its improved electrochemical properties for high-performance supercapacitors. *J. Power Sources* **2016**, *302*, 164–173.

[6] Wang, K.; Wu, H. P.; Meng, Y. N.; Wei, Z. X. Conducting polymer nanowire arrays for high performance supercapacitors. *Small* **2014**, *10*, 14–31.

[7] Shown, I.; Ganguly, A.; Chen, L. C.; Chen, K. H. Conducting polymer-based flexible supercapacitor. *Energy Sci. Eng.* **2015**, *3*, 2–26.

[8] Yu, X. Y.; Yu, L.; Shen, L. F.; Song, X. H.; Chen, H. Y.; Lou, X. W. General formation of MS (M = Ni, Cu, Mn) box-in-box hollow structures with enhanced pseudocapacitive properties. *Adv. Funct. Mater*. **2014**, *24*, 7440–7446.

[9] Yang, C.; Zhang, L. L.; Hu, N. T.; Yang, Z.; Wei, H.; Zhang, Y. F. Reduced graphene oxide/polypyrrole nanotube papers for flexible all-solid-state supercapacitors with excellent rate capability and high energy density. *J. Power Sources* **2016**, *302*, 39–45.

[10] Sun, X.; Guo, Y. Q.; Wu, C. Z.; Xie, Y. The hydric effect in inorganic nanomaterials for nanoelectronics and energy applications. *Adv. Mater*. **2015**, *27*, 3850–3867.

[11] Yu, C. F.; Ma, P. P.; Zhou, X.; Wang, A. Q.; Qian, T.; Wu, S. S.; Chen, Q. All-solid-state flexible supercapacitors based on highly dispersed polypyrrole nanowire and reduced graphene oxide composites. *ACS Appl. Mater. Interfaces* **2014**, *6*, 17937–17943.

[12] Yang, J. Q.; Duan, X. C.; Guo, W.; Li, D.; Zhang, H. L.; Zheng, W. J. Electrochemical performances investigation of NiS/rGO composite as electrode material for supercapacitors. *Nano Energy* **2014**, *5*, 74–81.

[13] Hou, L. R.; Yuan, C. Z.; Li, D. K.; Yang, L.; Shen, L. F.; Zhang, F.; Zhang, X. G. Electrochemically induced transformation of NiS nanoparticles into $Ni(OH)_2$ in KOH aqueous solution toward electrochemical capacitors. *Electrochim. Acta* **2011**, *56*, 7454–7459.

[14] Xing, Z. C.; Chu, Q. X.; Ren, X. B.; Tian, J. Q.; Asiri, A. M.; Alamry, K. A.; Al-Youbi, A. O.; Sun, X. P. Biomolecule-assisted synthesis of nickel sulfides/reduced graphene oxide nanocomposites as electrode materials for supercapacitors. *Electrochem. Commun*. **2013**, *32*, 9–13.

[15] Ma, L. B.; Shen, X. P.; Ji, Z. Y.; Wang, S.; Zhou, H.; Zhu, G. X. Carbon coated nickel sulfide/reduced graphene oxide nanocomposites: Facile synthesis and excellent supercapacitor performance. *Electrochim. Acta* **2014**, *146*, 525–532.

[16] Peng, L.; Ji, X.; Wan, H. Z.; Ruan, Y. J.; Xu, K.; Chen, C.; Miao, L.; Jiang, J. J. Nickel sulfide nanoparticles synthesized by microwave-assisted method as promising supercapacitor electrodes: An experimental and computational study. *Electrochim. Acta* **2015**, *182*, 361–367.

[17] Mahmood, N.; Zhang, C. Z.; Hou, Y. L. Nickel sulfide/nitrogen-doped graphene composites: Phase-controlled synthesis and high performance anode materials for lithium ion batteries. *Small* **2013**, *9*, 1321–1328.

[18] Gao, Y.; Mi, L. W.; Wei, W. T.; Cui, S. Z.; Zheng, Z.; Hou, H. W.; Chen, W. H. Double metal ions synergistic effect in hierarchical multiple sulfide microflowers for enhanced supercapacitor performance. *ACS Appl. Mater. Interfaces* **2015**, *7*, 4311–4319.

[19] Mei, L.; Yang, T.; Xu, C.; Zhang, M.; Chen, L. B.; Li, Q. H.; Wang, T. H. Hierarchical mushroom-like $CoNi_2S_4$ arrays as a novel electrode material for supercapacitors. *Nano Energy* **2014**, *3*, 36–45.

[20] Yang, J. Q.; Guo, W.; Li, D.; Qin, Q.; Zhang, J.; Wei, C. Y.; Fan, H. M.; Wu, L. Y.; Zheng, W. J. Hierarchical porous $NiCo_2S_4$ hexagonal plates: Formation via chemical conversion and application in high performance supercapacitors. *Electrochim. Acta* **2014**, *144*, 16–21.

[21] Nguyen, V. H.; Shim, J. J. *In situ* growth of hierarchical mesoporous $NiCo_2S_4$@MnO_2 arrays on nickel foam for high-performance supercapacitors. *Electrochim. Acta* **2015**, *166*, 302–309.

[22] Zhu, Y. R.; Wu, Z. B.; Jing, M. J.; Yang, X. M.; Song, W. X.; Ji, X. B. Mesoporous $NiCo_2S_4$ nanoparticles as high-performance electrode materials for supercapacitors. *J. Power Sources* **2015**, *273*, 584–590.

[23] Ratha, S.; Rout, C. S. Supercapacitor electrodes based on layered tungsten disulfide-reduced graphene oxide hybrids synthesized by a facile hydrothermal method. *ACS Appl. Mater. Interfaces* **2013**, *5*, 11427–11433.

[24] Li, Y. J.; Ye, K.; Cheng, K.; Yin, J. L.; Cao, D. X.; Wang, G. L. Electrodeposition of nickel sulfide on graphene-covered make-up cotton as a flexible electrode material for high-performance supercapacitors. *J. Power Sources* **2015**, *274*, 943–950.

[25] Yu, X. Y.; Yu, L.; Wu, H. B.; Lou, X. W. Formation of nickel sulfide nanoframes from metal–organic frameworks with enhanced pseudocapacitive and electrocatalytic properties. *Angew. Chem., Int. Ed.* **2015**, *54*, 5331–5335.

[26] Zhu, B.; Wang, Z. Y.; Ding, S. J.; Chen, J. S.; Lou, X. W. Hierarchical nickel sulfide hollow spheres for high performance supercapacitors. *RSC Adv*. **2011**, *1*, 397–400.

[27] Wang, Z.; Nan, C. Y.; Wang, D. S.; Li, Y. D. Fabrication of 1D nickel sulfide nanocrystals with high capacitances and remarkable durability. *RSC Adv*. **2014**, *4*, 47513–47516.

[28] Yang, J. Q.; Duan, X. C.; Qin, Q.; Zheng, W. J. Solvothermal synthesis of hierarchical flower-like β-NiS with excellent electrochemical performance for supercapacitors. *J. Mater. Chem. A* **2013**, *1*, 7880–7884.

[29] Yang, K. S.; Kim, B. H. Highly conductive, porous RuO_2/activated carbon nanofiber composites containing graphene for electrochemical capacitor electrodes. *Electrochim. Acta* **2015**, *186*, 337–344.

[30] Zhang, Z. M.; Zhao, C. J.; Min, S. D.; Qian, X. Z. A facile one-step route to RGO/Ni_3S_2 for high-performance supercapacitors. *Electrochim. Acta* **2014**, *144*, 100–110.

[31] Wang, A. M.; Wang, H. L.; Zhang, S. Y.; Mao, C. J.; Song, J. M.; Niu, H. L.; Jin, B. K.; Tian, Y. P. Controlled synthesis of nickel sulfide/graphene oxide nanocomposite for high-performance supercapacitor. *Appl. Surf. Sci*. **2013**, *282*, 704–708.

[32] Liu, X. J.; Qi, X.; Zhang, Z.; Ren, L.; Liu, Y. D.; Meng, L. J.; Huang, K.; Zhong, J. X. One-step electrochemical deposition of nickel sulfide/graphene and its use for supercapacitors. *Ceram. Int*. **2014**, *40*, 8189–8193.

[33] Cai, F.; Sun, R.; Kang, Y. R.; Chen, H. Y.; Chen, M. H.; Li, Q. W. One-step strategy to a three-dimensional NiS-reduced graphene oxide hybrid nanostructure for high performance supercapacitors. *RSC Adv*. **2015**, *5*, 23073–23079.

[34] Zhu, T.; Wu, H. B.; Wang, Y. B.; Xu, R.; Lou, X. W. Formation of 1D hierarchical structures composed of Ni_3S_2 nanosheets on CNTs backbone for supercapacitors and photocatalytic H_2 production. *Adv. Energy Mater*. **2012**, *2*, 1497–1502.

[35] Dai, C. S.; Chien, P. Y.; Lin, J. Y.; Chou, S. W.; Wu, W. K.; Li, P. H.; Wu, K. Y.; Lin, T. W. Hierarchically structured Ni_3S_2/carbon nanotube composites as high performance cathode materials for asymmetric supercapacitors. *ACS Appl. Mater. Interfaces* **2013**, *5*, 12168–12174.

[36] Singh, A.; Roberts, A. J.; Slade, R. C. T.; Chandra, A. High electrochemical performance in asymmetric supercapacitors using MWCNT/nickel sulfide composite and graphene nanoplatelets as electrodes. *J. Mater. Chem. A* **2014**, *2*, 16723–16730.

[37] Yan, J.; Lui, G.; Tjandra, R.; Wang, X. L.; Rasenthiram, L.; Yu, A. P. α-NiS grown on reduced graphene oxide and single-wall carbon nanotubes as electrode materials for high-power supercapacitors. *RSC Adv*. **2015**, *5*, 27940–27945.

[38] Yu, W. D.; Lin, W. R.; Shao, X. F.; Hu, Z. X.; Li, R. C.; Yuan, D. S. High performance supercapacitor based on Ni_3S_2/carbon nanofibers and carbon nanofibers electrodes derived from bacterial cellulose. *J. Power Sources* **2014**, *272*, 137–143.

[39] Wang, Z. Q.; Li, X.; Yang, Y.; Cui, Y. J.; Pan, H. G.; Wang, Z. Y.; Chen, B. L.; Qian, G. D. Highly dispersed β-NiS nanoparticles in porous carbon matrices by a template metal–organic framework method for lithium-ion cathode. *J. Mater. Chem. A* **2014**, *2*, 7912–7916.

[40] Chen, Y. P.; Liu, B. R.; Jiang, W.; Liu, Q.; Liu, J. Y.; Wang, J.; Zhang, H. S.; Jing, X. Y. Coaxial three-dimensional $CoMoO_4$ nanowire arrays with conductive coating on carbon cloth for high-performance lithium ion battery anode. *J. Power Sources* **2015**, *300*, 132–138.

[41] Zhang, H. M.; Yu, X. Z.; Guo, D.; Qu, B. H.; Zhang, M.; Li, Q. H.; Wang, T. H. Synthesis of bacteria promoted reduced graphene oxide-nickel sulfide networks for advanced supercapacitors. *ACS Appl. Mater. Interfaces* **2013**, *5*, 7335–7340.

[42] Xu, Y. X.; Sheng, K. X.; Li, C.; Shi, G. Q. Self-assembled graphene hydrogel via a one-step hydrothermal process. *ACS Nano* **2010**, *4*, 4324–4330.

[43] Sheng, K. X.; Xu, Y. X.; Li, C.; Shi, G. Q. High-performance self-assembled graphene hydrogels prepared by chemical reduction of graphene oxide. *New Carbon Mater*. **2011**, *26*, 9–15.

[44] Xu, Y. X.; Lin, Z. Y.; Huang, X. Q.; Liu, Y.; Huang, Y.; Duan, X. F. Flexible solid-state supercapacitors based on three-dimensional graphene hydrogel films. *ACS Nano* **2013**, *7*, 4042–4049.

[45] Sui, Z. Y.; Meng, Y. N.; Xiao, P. W.; Zhao, Z. Q.; Wei, Z. X.; Han, B. H. Nitrogen-doped graphene aerogels as efficient supercapacitor electrodes and gas adsorbents. *ACS Appl. Mater. Interfaces* **2015**, *7*, 1431–1438.

[46] Sun, H. Y.; Xu, Z.; Gao, C. Multifunctional, ultra-flyweight, synergistically assembled carbon aerogels. *Adv. Mater*. **2013**, *25*, 2554–2560.

[47] Van Aken, K. L.; Pérez, C. R.; Oh, Y.; Beidaghi, M.; Jeong, Y. J.; Islam, M. F.; Gogotsi, Y. High rate capacitive performance of single-walled carbon nanotube aerogels. *Nano Energy* **2015**, *15*, 662–669.

[48] Wang, C. H.; He, X. D.; Shang, Y. Y.; Peng, Q. Y.; Qin, Y. Y.; Shi, E. Z.; Yang, Y. B.; Wu, S. T.; Xu, W. J.; Du, S. Y. et al. Multifunctional graphene sheet-nanoribbon hybrid aerogels. *J. Mater. Chem. A* **2014**, *2*, 14994–15000.

[49] Chen, L.; Du, R.; Zhu, J. H.; Mao, Y. Y.; Xue, C.; Zhang, N.; Hou, Y. L.; Zhang, J.; Yi, T. Three-dimensional nitrogen-doped graphene nanoribbons aerogel as a highly efficient catalyst for the oxygen reduction reaction. *Small* **2015**, *11*, 1423–1429.

[50] Zhang, Y. F.; Fan, W.; Huang, Y. P.; Zhang, C.; Liu, T. X.

Graphene/carbon aerogels derived from graphene crosslinked polyimide as electrode materials for supercapacitors. *RSC Adv*. **2015**, *5*, 1301–1308.

[51] Liu, R. L.; Wan, L.; Liu, S. Q.; Pan, L. X.; Wu, D. Q.; Zhao, D. Y. An interface-induced co-assembly approach towards ordered mesoporous carbon/graphene aerogel for high-performance supercapacitors. *Adv. Funct. Mater*. **2015**, *25*, 526–533.

[52] Zuo, L. Z.; Zhang, Y. F.; Zhang, L. S.; Miao, Y. E.; Fan, W.; Liu, T. X. Polymer/carbon-based hybrid aerogels: Preparation, properties and applications. *Materials* **2015**, *8*, 6806–6848.

[53] Xu, X. Z.; Zhou, J.; Nagaraju, D. H.; Jiang, L.; Marinov, V. R.; Lubineau, G.; Alshareef, H. N.; Oh, M. Flexible, highly graphitized carbon aerogels based on bacterial cellulose/lignin: Catalyst-free synthesis and its application in energy storage devices. *Adv. Funct. Mater*. **2015**, *25*, 3193–3202.

[54] Bi, H. C.; Yin, Z. Y.; Cao, X. H.; Xie, X.; Tan, C. L.; Huang, X.; Chen, B.; Chen, F. C.; Yang, Q. L.; Bu, X. Y. et al. Carbon fiber aerogel made from raw cotton: A novel, efficient and recyclable sorbent for oils and organic solvents. *Adv. Mater*. **2013**, *25*, 5916–5921.

[55] Fan, W.; Xia, Y. Y.; Tjiu, W. W.; Pallathadka, P. K.; He, C. B.; Liu, T. X. Nitrogen-doped graphene hollow nanospheres as novel electrode materials for supercapacitor applications. *J. Power Sources* **2013**, *243*, 973–981.

[56] Mahmood, N.; Tahir, M.; Mahmood, A.; Zhu, J. H.; Cao, C. B.; Hou, Y. L. Chlorine-doped carbonated cobalt hydroxide for supercapacitors with enormously high pseudocapacitive performance and energy density. *Nano Energy* **2015**, *11*, 267–276.

[57] Yin, H.; Zhang, C. Z.; Liu, F.; Hou, Y. L. Hybrid of iron nitride and nitrogen-doped graphene aerogel as synergistic catalyst for oxygen reduction reaction. *Adv. Funct. Mater*. **2014**, *24*, 2930–2937.

[58] Yan, J. J.; Huang, Y. P.; Miao, Y. E.; Tjiu, W. W.; Liu, T. X. Polydopamine-coated electrospun poly(vinyl alcohol)/poly(acrylic acid) membranes as efficient dye adsorbent with good recyclability. *J. Hazard. Mater*. **2015**, *283*, 730–739.

[59] Jeong, H. M.; Lee, J. W.; Shin, W. H.; Choi, Y. J.; Shin, H. J.; Kang, J. K.; Choi, J. W. Nitrogen-doped graphene for high-performance ultracapacitors and the importance of nitrogen-doped sites at basal planes. *Nano Lett*. **2011**, *11*, 2472–2477.

[60] Sun, C. C.; Ma, M. Z.; Yang, J.; Zhang, Y. F.; Chen, P.; Huang, W.; Dong, X. C. Phase-controlled synthesis of α-NiS nanoparticles confined in carbon nanorods for high performance supercapacitors. *Sci. Rep*. **2014**, *4*, 7054.

[61] Yang, J. Q.; Guo, W.; Li, D.; Wei, C. Y.; Fan, H. M.; Wu, L. Y.; Zheng, W. J. Synthesis and electrochemical performances of novel hierarchical flower-like nickel sulfide with tunable number of composed nanoplates. *J. Power Sources* **2014**, *268*, 113–120.

[62] Zhang, Y.; Sun, W. P.; Rui, X. H.; Li, B.; Tan, H. T.; Guo, G. L.; Madhavi, S.; Zong, Y.; Yan, Q. Y. One-pot synthesis of tunable crystalline Ni_3S_4@amorphous MoS_2 core/shell nanospheres for high-performance supercapacitors. *Small* **2015**, *11*, 3694–3702.

Table of contents

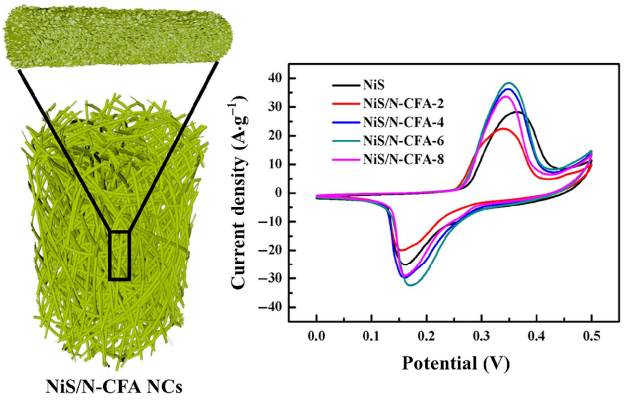

N-doped carbon fiber aerogel-supported NiS nanoparticles were utilized as excellent electrode materials for supercapacitors.

Electronic Supplementary Material

Immobilization of NiS nanoparticles on N-doped carbon fiber aerogels as advanced electrode materials for supercapacitors

Youfang Zhang[1], Lizeng Zuo[1], Longsheng Zhang[1], Jiajie Yan[1], Hengyi Lu[1], Wei Fan[2] (✉), and Tianxi Liu[1,2] (✉)

[1] *State Key Laboratory of Molecular Engineering of Polymers, Department of Macromolecular Science, Fudan University, 220 Handan Road, Shanghai 200433, China*

[2] *State Key Laboratory of Modification of Chemical Fibers and Polymer Materials, College of Materials Science and Engineering, Donghua University, 2999 North Renmin Road, Shanghai 201620, China*

Supporting information to DOI 10.1007/s12274-016-1163-1

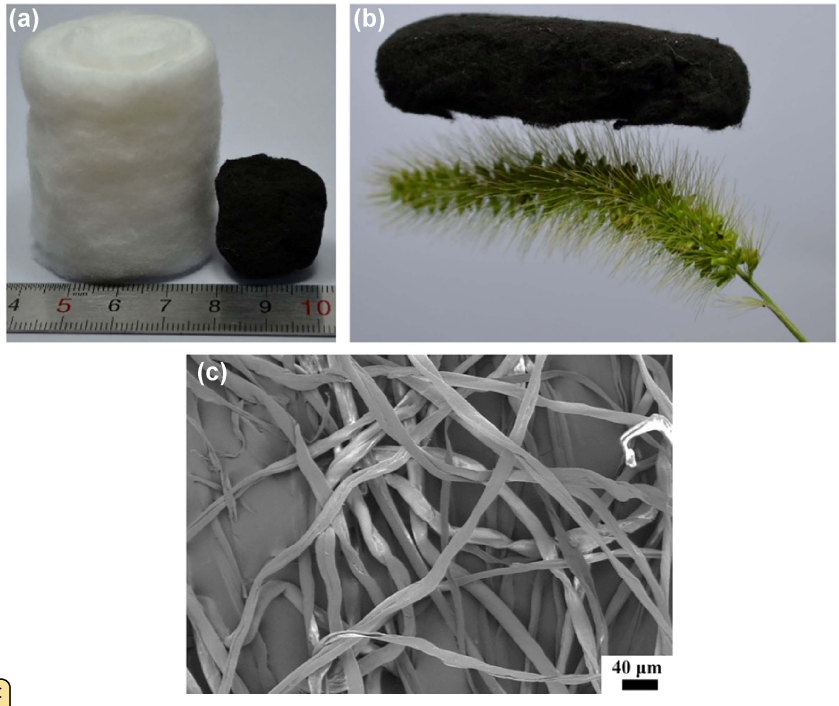

Figure S1 FESEM images of a cotton wool before (left) and after carbonization (right) (a), and the digital photograph of a CFA on a green bristle grass (b). FESEM image of cotton wool (c).

Address correspondence to Wei Fan, weifan@dhu.edu.cn; Tianxi Liu, txliu@fudan.edu.cn, txliu@dhu.edu.cn

Figure S2 The digital photograph of raw cotton wool before and after PDA coating.

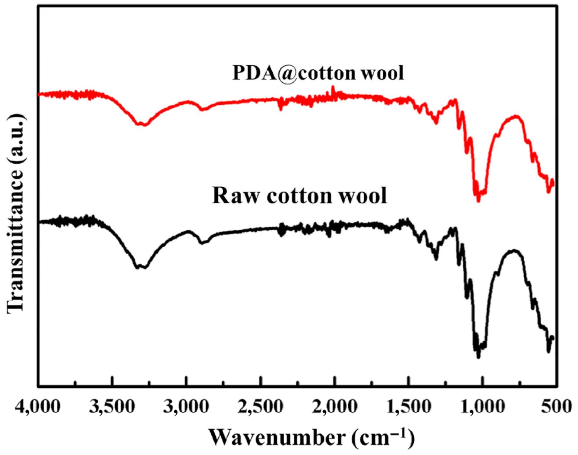

Figure S3 FTIR spectra of raw cotton wool and PDA@cotton wool.

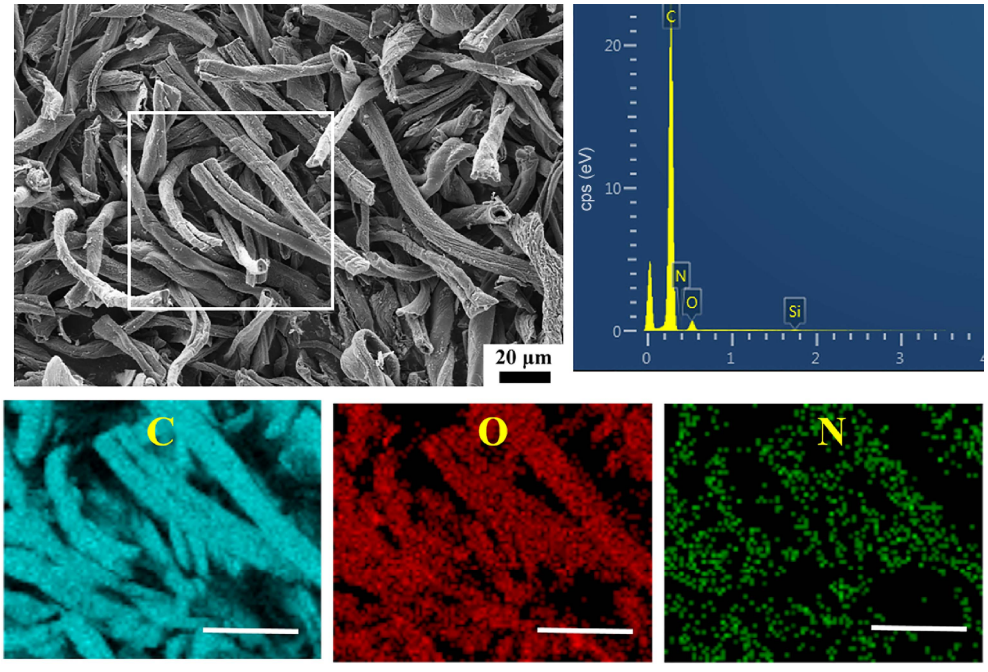

Figure S4 The EDS mapping of N-CFA (scale bar: 25 μm).

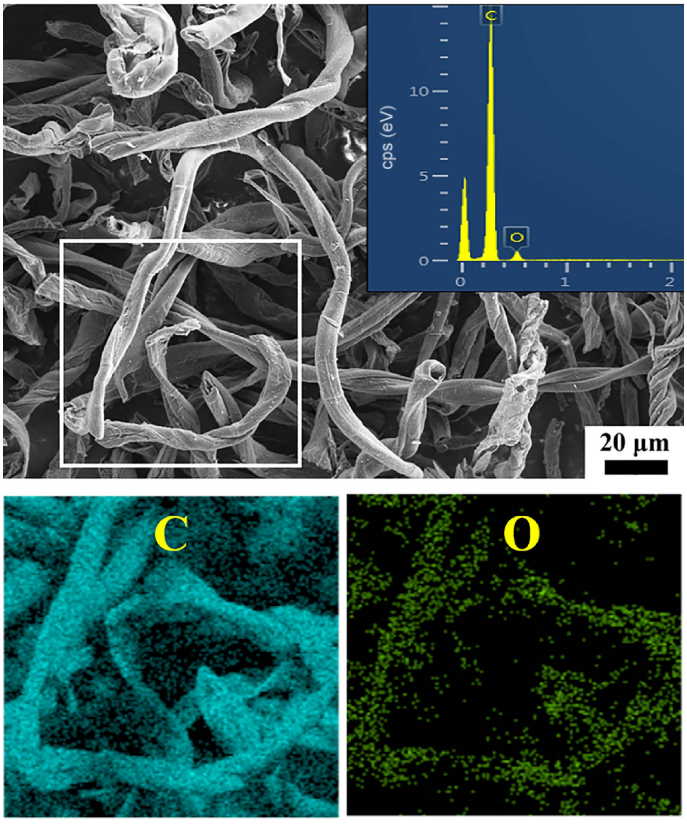

Figure S5 The EDS mapping of CFA (scale bar: 25 μm).

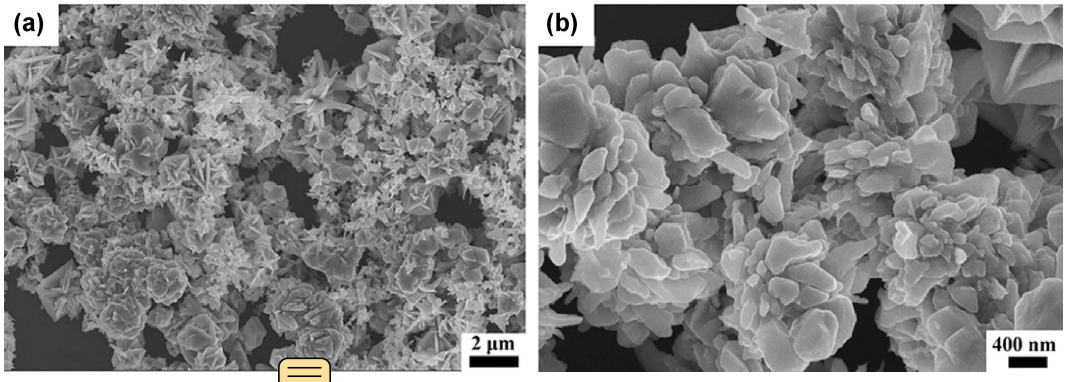

Figure S6 FESEM images of NiS nanoparticles at low (a) and high (b) magnifications.

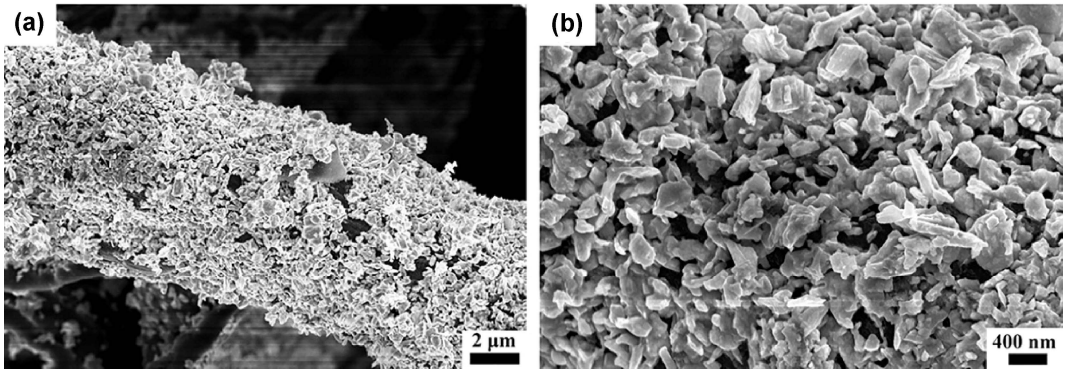

Figure S7 FESEM images of NiS/CFA-6 at low (a) and high (b) magnifications.

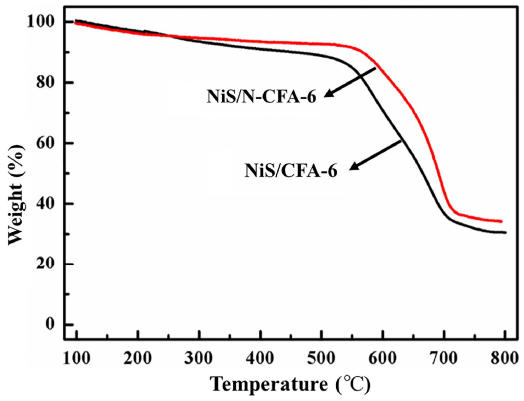

Figure S8 TGA curves of NiS/CFA-6 and NiS/N-CFA-6.

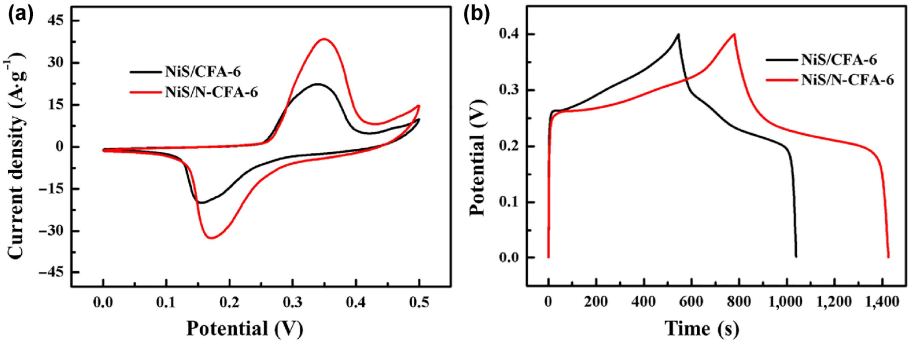

Figure S9 CV curves of NiS/CFA-6 and NiS/N-CFA-6 at a scan rate of 10 $mV \cdot s^{-1}$ (a) and galvanostatic charge–discharge curves at current density of 1 $A \cdot g^{-1}$ (b).

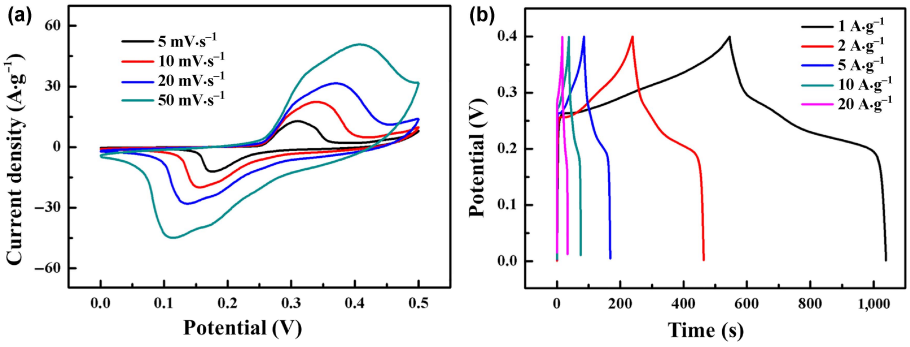

Figure S10 Rate capabilities of NiS/CFA-6 nanocomposite at various scan rates and current densities.

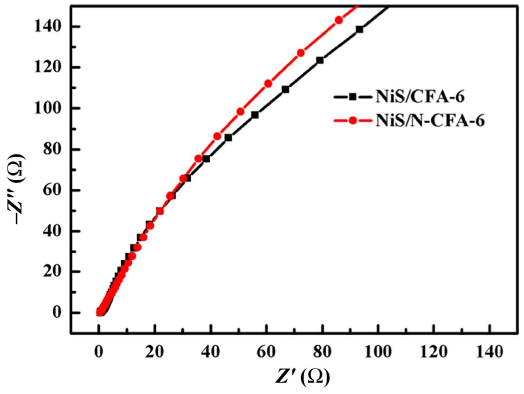

Figure S11 Nyquist plots of NiS/CFA-6 nanocomposite measured in frequency range from 100 kHz to 0.01 Hz.